Dual Frequency Hierarchical Modular Multilayer Battery Balancer Architecture

Ming Liu, *Member, IEEE*, Yenan Chen, *Member, IEEE*, Youssef Elasser, *Student Member, IEEE*, and Minjie Chen, *Senior Member, IEEE*

***Abstract*—This article presents a dual frequency hierarchical modular multilayer balancer (MMB) architecture capable of performing electrochemical impedance spectroscopy (EIS) and self-heating for battery systems. The MMB comprises two layers of balancing circuits: a cell-level balancer operates at a few MHz with miniaturized size; and a string-level balancer operates at a few hundred kHz to achieve high efficiency and rapid balancing. By reusing the balancer circuitry, the cell-level balancer can perform EIS, and the string-level balancer can perform battery self-heating. The key contributions of this article include: first, the circuit topology and multi-input–multi-output (MIMO) power flow control of the dual frequency hierarchical balancer; second, a miniaturized common-mode (CM) Class-D based 4-port cell-level balancer for wide bandwidth EIS; and third, a high efficiency multiactive-bridge (MAB) based 12-port string-level balancer for self-heating. A MMB prototype with a 12-port 200 kHz string-level balancer and four 4-port 13.56 MHz cell-level balancers is built and tested with a battery string comprising sixteen Li-ion battery cells. The MMB is capable of performing EIS up to 100 kHz and self-heating across a wide frequency range (100 Hz–18 kHz). The 100-W 12-port string-level balancer achieves 93% peak efficiency. The 30-W 4-port cell-level balancer achieves 74% peak efficiency. Experimental results validated the performance and functionality of the MMB system.**

***Index Terms*—Battery management system (BMS), common-mode class-d converter, electrochemical impedance spectroscopy (EIS), multiactive-bridge (MAB) converter, multi-input–multi-output (MIMO), multiport power electronics, power flow control, self-heating.**

I. Introduction

ELECTROCHEMICAL energy storage are becoming increasingly important as the rapid development of electric vehicles and renewable energy [1]–[4]. Battery systems need higher density, higher efficiency, and longer lifetime. High performance Li-ion battery systems usually comprise strings of battery cells to achieve high output voltage and high power rating [5], [6]. After repeated charging and discharging, the numerous battery cells inevitably have different state-of-charge (SOC) and state-of-health (SOH). The charge imbalance among the battery cells limits the life-cycle and energy capacity of the full battery system [7], [8]. Battery management systems (BMS) can monitor the SOC and SOH of the batteries and extend the battery lifetime [9]–[11]. They are important building blocks of electric vehicles and grid scale energy storage systems.

Impedance based estimation methods such as electrochemical impedance spectroscopy (EIS) are promising techniques to infer the battery SOC and SOH [12]–[18]. By using EIS, the various electrochemical phenomena of the battery can be observed and analyzed in the frequency domain. Fig. 1(a) shows the measured Nyquist curves of a Li-ion battery LIR2032 with different SOC. The low frequency ($<$1 Hz) patterns of the Nyquist curve reflects the mass-transport effects; the medium frequency (1 Hz to 1 kHz) patterns reflects the charge-transfer effects; and the high frequency range ($>$1 kHz) patterns reflects the conductance effects. EIS results across the entire frequency range are valuable for SOC and SOH estimation. Fig. 1(b) shows the Nyquist plot of a lithium-ion battery ICR18650 in different temperatures. It shows that the battery impedance changes with the varying temperatures.

Li-ion batteries can rapidly degrade if heavily operated in low temperature, due to the reduced electrolyte conductivity [19], reduced solid-state Li-ion diffusivity [20], and the sluggish kinetics of charge transfer [21]. Preheating the battery before heavy operation in cold temperature is necessary to improve the performance and extend the lifetime of batteries. There are two general ways of preheating Li-ion batteries: first, passive preheating; and second, active preheating. In passive preheating, heat is generated by an external source and mechanically propagates through batteries. Passive preheating is simple to implement, but requires additional infrastructure and cannot guarantee uniform temperature raise in batteries. Active preheating, as an additional function of the BMS, can smoothly heat the battery by the ohmic-loss and electrochemical heat. Different active heating strategies have been investigated to increase the heating speed with less impact on the battery performance [22]–[25]. A 10 to 20 kHz ac current active heater for hybrid EV battery was introduced in [26], where a half-bridge inverter powered by the

Manuscript received March 18, 2020; revised June 20, 2020; accepted July 27, 2020. Date of publication August 11, 2020; date of current version October 30, 2020. This work was supported in part by the National Science Foundation, DOE ARPA-E CIRCUITS Program, in part by the Princeton E-ffiliates Program and in part by the Princeton E-ffiliates Partnership program, DOE ARPA-E CIRCUITS Program, and in part by the National Science Foundation under Grant 1847365. This paper was presented in part at the IEEE Energy Conversion Congress and Exposition, Baltimore, MD, USA, September 2019, and in part by the 20th Workshop on Control and Modeling for Power Electronics, Toronto, ON, Canada, June 16–19, 2019. Recommended for publication by Associate Editor H. Hofmann. *(Corresponding author: Minjie Chen.)*

The authors are with the Department of Electrical Engineering and Andlinger Center for Energy and the Environment, Princeton University, Princeton, NJ 08540 USA (e-mail: ml45@princeton.edu; yenanc@princeton.edu; yelasser@princeton.edu; minjie@princeton.edu).

Color versions of one or more of the figures in this article are available online at https://ieeexplore.ieee.org.

Digital Object Identifier 10.1109/TPEL.2020.3015768

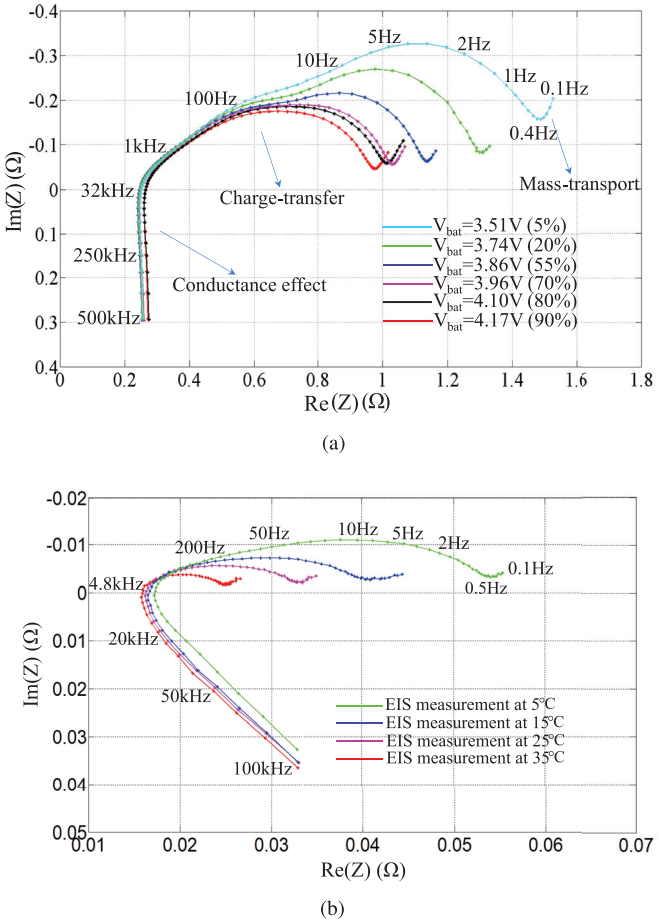

Fig. 1. (a) Measured Nyquist curves of a Li-ion rechargeable coin battery LIR2032 with different SOC. (b) Measured Nyquist curves of a Li-ion rechargeable battery ICR18650 under different temperatures using a Gamry Reference 600 Analyzer.

onboard generator is used as the active heater. Shang *et al.* [27] proposed a buck–boost converter based active heater by using the battery pack to power the heater itself. Shang *et al.*[28] discussed an integrated heater-equalizer which achieves the internal and external combined heating as well as passive equalization for battery strings. A half-bridge active heater with soft switching operation and a resonant switched-capacitor heater with compact structure were presented for the battery active preheating applications in [29] and [30].

Existing battery balancer circuits are usually implemented as multiport dc-link systems, which utilize dc-link capacitors to transfer energy [31]–[33]. As shown in Fig. 2(a) and (b), the load to load balancer and the switched-capacitor balancer are ladder converters, and they can only process the differential power between two neighboring battery cells in one switching-cycle. Fig. 2(c) shows the block diagrams of a dc-coupled battery balancer, which transfers power directly between two arbitrary battery cells through two "dc–ac–dc" conversion stages. In these balancers, the power flow between two battery cells needs to be processed by more than one "dc–ac–dc" power stages. Fig. 2(d) shows a MAC (multiwinding transformer) converters, which can process the differential power of the two battery cells only through one "dc–ac–dc" conversion stage [34]. This converter can provide reduced power conversion stress and low component count for battery balancing operation, but the control is complicated because all of the cells are coupled via one MAC transformer, especially with a large number of battery cells.

This article presents a dual frequency multilayer battery balancer architecture with multi-input–multi-output (MIMO) power flow control. This is the first demonstration of a multilayer battery balancer system with EIS and self-heating functions by reusing the battery balancer circuitry. It comprises a 13.56 MHz miniaturized common-mode (CM) Class-D based cell-level balancer for wide bandwidth EIS; and a 200 kHz high efficiency multiactive-bridge (MAB) based string-level balancer for rapid balancing and self-heating. Compared to other existing work on hierarchical multilayer battery balancer [35]–[39], the proposed dual frequency approach offers: first, miniaturized magnetic size of the cell-level balancer due to the high frequency operation (13.56 MHz) and air coupling; second, improved efficiency of the string-level balancer benefiting from the MAB topology; third, EIS measurement and self-heating capabilities enabled by the MAC topology and MIMO power flow control. The proposed architecture is capable of performing many battery management functions at the same time. For example, based on the EIS estimation of the SOC and SOH of battery cells, one can determine the optimal power flow control strategy to balance the SOC and SOH of the battery cells while performing self-heating with minimum battery degradation.

The remainder of this article is organized as follows. Section II provides an overview of the MMB architecture. Section III-A discusses the balancing operation of the MMB architecture and the multiway MIMO power flow. Section IV discusses the multiwinding transformers design of the kHz MAB-based string-level balancer and the MHz CM Class-D based cell-level balancer. Section V discusses the implementation details of the EIS and the battery self-heating functions. Section VI shows the design of the prototype and experimental results, and demonstrates the functions of multilayer battery balancing, battery EIS, and self-heating. Finally, Section VII concludes this article.

II. Architecture and Topology Overview

Fig. 3 shows the key principles of the MMB architecture. Multiple battery cells are grouped into multiple series-connected battery strings. Multiple battery strings are connected in series to create battery packs. Cell-to-cell and string-to-string power flow co-exist in the balancing process. There are many ways of implementing the MAC converters [40]–[43]. The example topology in Fig. 3 consists of two layers of MAC converters, i.e., a cell-level balancer and a string-level balancer. The string-level balancer switches at a few hundred kHz and performs string-level self-heating. The cell-level balancer switches at a few MHz and performs cell-level EIS. One inverter topology works at a few hundred kHz and drives a kHz multiwinding transformer as the string-level balancer. Another inverter topology works at a few MHz and drives a MHz multiwinding transformer (air-coupled for miniaturized size) as the cell-level balancer.

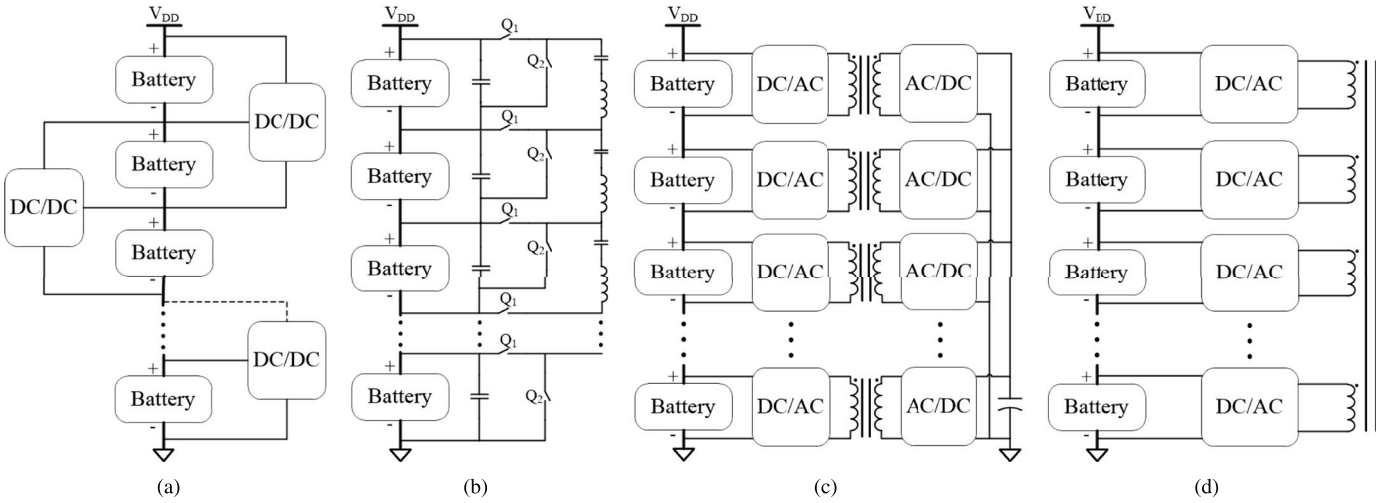

Fig. 2. Block diagrams of a few battery balancer topologies [3]. (a) Load-to-load battery balancer. (b) Switched-capacitor battery balancer. (c) DC-coupled battery balancer. (d) Multiport-ac-coupled (MAC) battery balancer. The MAC battery balancer is attractive due to the reduced power conversion stress. There is only one "dc–ac–dc" power conversion stage between two arbitrary battery cells.

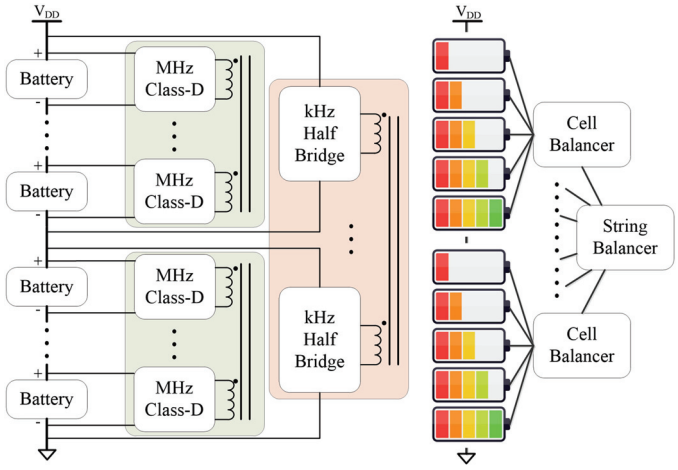

Fig. 3. Dual frequency modular multilayer balancer (MMB) architecture comprises two types of balancing circuits operating at two frequencies: one at high frequency (MHz) performs cell-level balancing and EIS, and the other at low frequency (kHz) performs self-heating and string-level balancing.

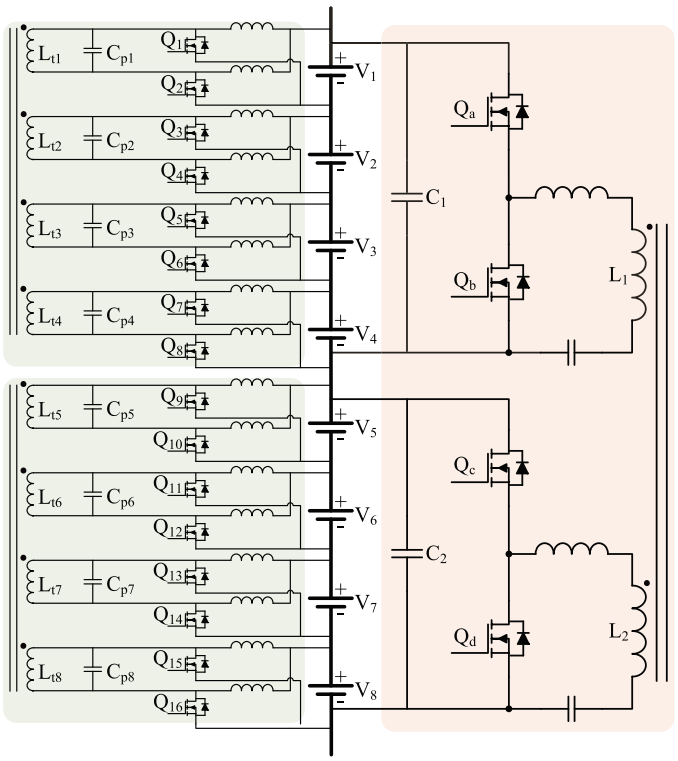

Fig. 4. Topology of an example dual frequency MMB with two 4-port 13.56 MHz cell-level balancers with EIS capability; and one 2-port 200 kHz string-level balancer with self-heating capability.

The benefits of the MMB architecture include: first, the battery strings are grouped into multiple layers, e.g., the string-level layer and the cell-level layer, which eliminates the coupling influence among the cells in different strings and highly reduces the complicity and control of a fully coupled battery balancer architecture where all battery cells are directly coupled [42]; second, it enables different balancing frequencies at different layers. The cell-level balancer switches at a few MHz for reduced size and miniaturized packaging. The string-level balancer switches at a few hundred kHz for improved efficiency and faster balancing; third the dual frequency multiway MIMO power flow enables cell-level EIS and string-level self-heating by reusing the battery balancer circuitry.

Fig. 4 shows the topology of an example MMB. A 2-port MAB converter is used for string-to-string balancing. It consists of two half-bridge inverters and a 2-winding transformer. Each battery string comprises four battery cells. In the MAB converter, energy is delivered from one port to another, or from multiple input ports to multiple output ports through phase shift. The MAB converter was designed to operated at a few hundred kHz. Other MAC topologies (e.g., LLC, DAB) are also applicable. The cell-level balancers are implemented as two 4-port

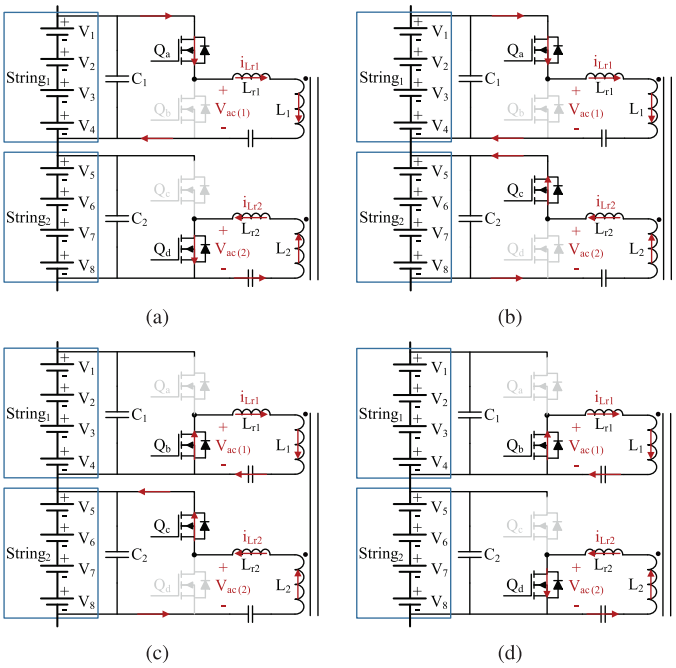

Fig. 5. Operation principles of the kHz string-level balancer when the power is transferred from battery string #1 to battery string #2: (a) State I. (b) State II. (c) State III. (d) State IV.

common-mode (CM) Class-D converters. The two switches in one CM Class-D inverter are working 180° out of phase with 50% duty cycle. The cell-level balancer was designed to switch at a few MHz to minimize the size of the multiwinding transformer. The example MMB can be easily extended for a large scale of batteries balancing application by using a multiport kHz MAB converter and multiple MHz CM Class-D converters.

III. Operation Principle and Power Flow Control

The MMB architecture processes multilayer, multiway, multifrequency, and MIMO power flow. Here, we introduce the operation principles and power flow control of the kHz string-level balancer and the MHz cell-level balancer.

A. Operation of the kHz String-Level Balancer

Fig. 5 shows the operation principles of the string-level balancer when power is transferred from string #1 to string #2. Fig. 6 shows the key operation waveforms of the string-level balancer. Similar to a MAB converter, the switching cycle is divided into four intervals based on the inductor current waveform and phase shift between the voltages across the transformer. In State I (t_0–t_1), switches Q_a and Q_d are turned ON and the inductor current i_{Lr1} is changed from negative to positive during this state. In State II (t_1–t_2), switches Q_a and Q_c are turned ON and the inductor current i_{Lr1} continues to flow into the transformer, discharging battery string #1 and charging battery string #2. In State III (t_2–t_3), switches Q_b and Q_c are turned ON and the inductor current i_{Lr1} is changed from positive to negative. In State IV (t_3–t_4), switches Q_b and Q_d are turned ON and the inductor current i_{Lr1} is circulating through switches Q_b and Q_d

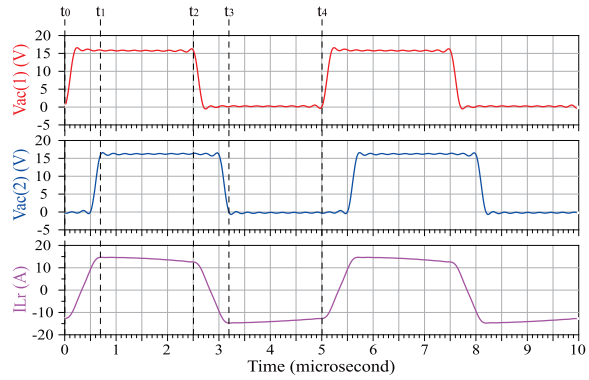

Fig. 6. Key waveforms of the kHz string-level balancer operating at 200 kHz.

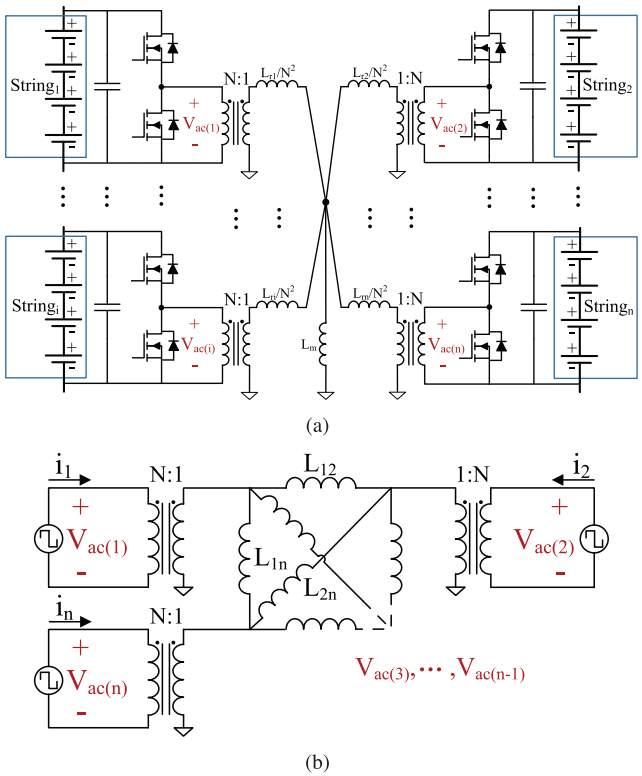

Fig. 7. (a) Lumped circuit model of the n-port kHz string-level balancer with a Star model of the multiwinding transformer. (b) Lumped circuit model of the n-port string-level balancer with the cantilever model of the multiwinding transformer and multiple square wave voltage sources.

on the primary and secondary sides. The current waveforms are trapezoidal.

The string-level balancer functions as an MAB converter. It can be modeled as an n-port (n-winding) transformer with n square wave voltage sources, as shown in Fig. 7(a). Each winding has N turns. The series-connected blocking capacitors are large enough and are neglected in the analysis. L_{r1}–L_{r4} are represented as the normalized inductance per-turn (L_{ri}/N^2) in the star model and L_m is the magnetizing inductance. The Star model can be converted into an equivalent delta model or a cantilever model to simplify the power flow analysis [43], as

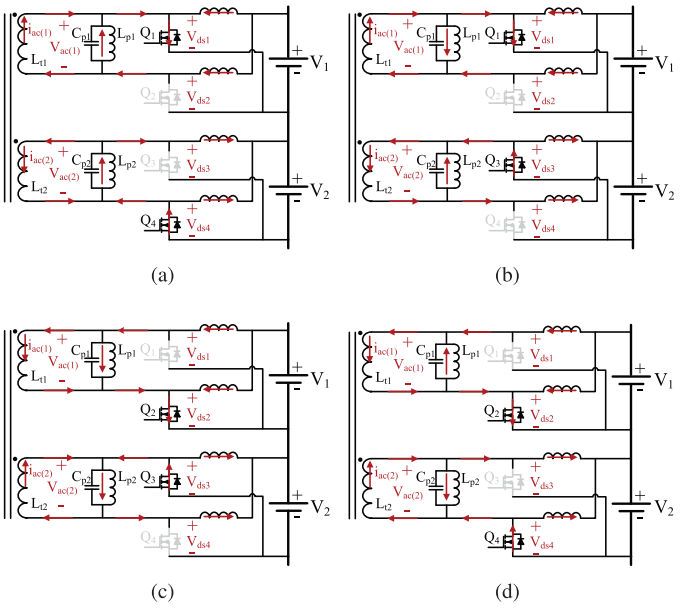

Fig. 8. Operation principles of the MHz cell-level balancer when the power is transferred from cell #1 to cell #2: (a) State I. (b) State II. (c) State III. (d) State IV.

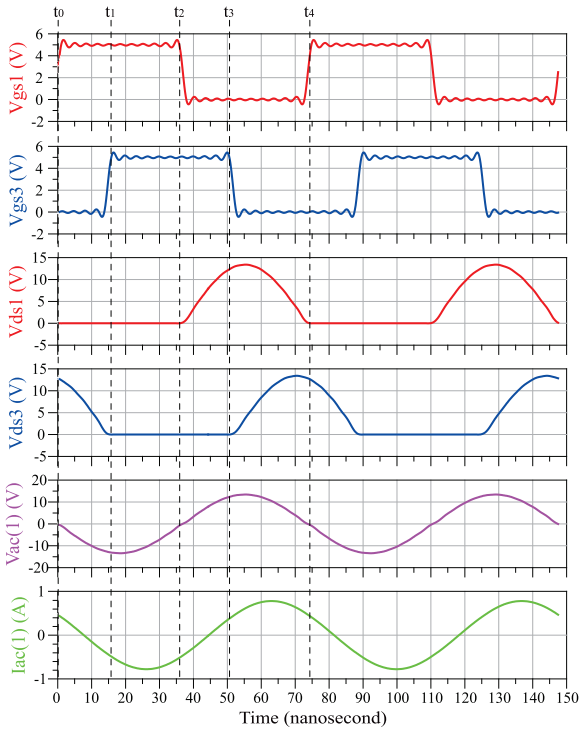

Fig. 9. Key waveforms of the cell-level balancer operating at 13.56 MHz.

shown in Fig. 7(b). The n half-bridge inverters are modeled as n square wave voltage sources $V_{\text{ac}(1)}$–$V_{\text{ac}(n)}$. Based on Fig. 7, the power fed into an arbitrary port k is

$$P_k^V = V_{\text{ac}(k)} \times i_k^* = \frac{V_{\text{ac}(k)}}{N^2} \sum_{q=1,q\neq k}^{n} \frac{V_{\text{ac}(q)}}{\omega L_{qk}} \phi_{qk} \left(1 - \frac{\phi_{qk}}{\pi}\right). \tag{1}$$

The multiway power flow in the MAB converter can be controlled to implement the MIMO balancing operation by modulating the voltage phase shift of all ports, i.e., the phases of $V_{\text{ac}(1)}$–$V_{\text{ac}(n)}$. As demonstrated in [40], a dedicated distributed phase shift controller can be implemented at each port to modulate the power processed by each port without a central control command.

B. Operation Principles of the MHz Cell-Level Balancer

Fig. 8 shows the operation principles of the MHz cell-level balancer when the power is transferred from cell #1 to cell #2. The working state is divided into four intervals based on the switching patterns: switches Q_1 and Q_4 conduct in State I (t_0–t_1); switches Q_1 and Q_3 conduct in State II (t_1–t_2); switches Q_2 and Q_3 conduct at State III (t_2–t_3); switches Q_2 and Q_4 conduct in State IV (t_3–t_4). Fig. 9 shows the key waveforms of the MHz cell-level balancer. The gate drive voltage and drain-source voltage waveforms of switch Q_2 and Q_4 are not shown in Fig. 9 and their waveforms are same as the waveforms of Q_1 and Q_3 with an 180° phase shift because of the complementary switching. Note the parallel inductors L_{p1} and L_{p2} can be absorbed into the transformer winding with a proper parameter selection. As shown in Figs. 8 and 9, with a phase shift ϕ, the output current of battery Cell #1 flows through the parallel resonant tank $L_{p1} - C_{p1}$, which shapes the sinusoidal waveform of $V_{\text{ac}(1)}$ and provides a sinusoidal current into the transformer and deliver power to cell #2.

The MHz CM Class-D inverters function as current sources instead of voltage sources. The full-order cantilever model is not suitable to model and control the multiway MIMO power flow. An alternative way to model the n-port current-source driven multiwinding transformer is to simplify the cantilever model into an inductive coupled model, where all ports are driven by sinusoidal current source inverters. Thus, a CM Class-D balancer with n battery cells is modeled as an n-port inductive coupled model with n sinusoidal current sources to analyze its multiway balancing operation, as shown in Fig. 10. The coupling between any two arbitrary coils is described by their mutual inductance. Here, L_i is the self-inductance of the ith coil and L_{ij} is the mutual inductance between the ith and jth coils. Based on this simplified cantilever model, the power fed into port k is

$$P_k^I = V_k \times i_k^* = \frac{1}{2} \sum_{q=1,q\neq k}^{n} \omega L_{qk} I_{\text{ac}(k)} I_{\text{ac}(q)} \sin\phi_{qk} \tag{2}$$

where i_k^* is the conjugate current of i_k. $I_{\text{ac}(k)}$ and $I_{\text{ac}(q)}$ are the magnitudes of the currents at port k and port q, respectively. ϕ_{qk} is the phase difference between the current of port q and port k. Equation (2) indicates that the multiway power flow in the current source driven multiwinding transformer can be controlled in a similar way as the power flow in a voltage source driven multiwinding transformer, with a different set of power flow equations. Note the multiway balancing operation analysis above can be also applied to other balancers with a multiwinding

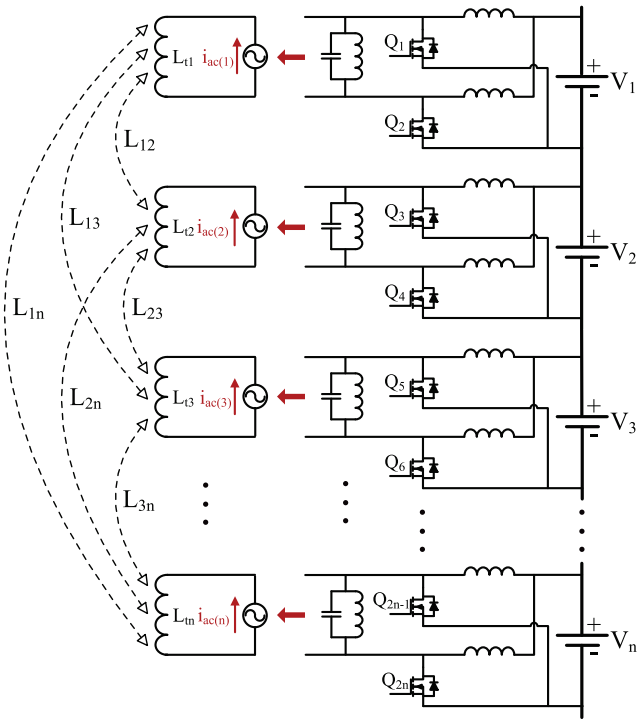

Fig. 10. Lumped circuit model of the n-port MHz cell-level balancer with the inductive coupled model of the multiwinding transformer and multiple sinusoidal current sources.

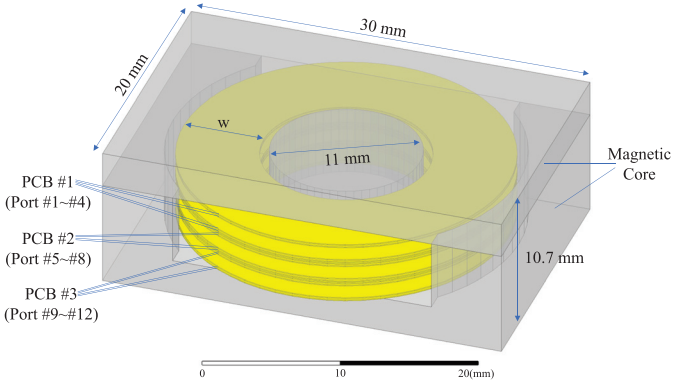

Fig. 11. FEM of the 200 kHz 12-winding transformer implemented on three FR4 PCBs.

transformer and multiple inverters which function as current sources.

IV. Multiwinding Transformer Design

In the MMB architecture, power is routed on the string-level through the kHz MAB converter, and on the cell-level through the MHz CM Class-D inverters. The performance of the multiwinding transformer determines the efficiency and power transfer capability of both balancers. Fig. 11 shows the finite-element-model (FEM) of a 12-port 200 kHz multiwinding transformer. The transformer consists of a magnetic core and three vertical-stacked printed circuit boards (PCBs) each

TABLE I
Parameters of the kHz Multiwinding Transformer

Transformer Parameters (200 kHz)	Description
Number of turns (N)	1
Trace width (w)	7.5 mm
Trace thickness	70 μm
Magnetic core	Ferroxcube-EQ/PLT30/3F3
L_i (i=1-12)	9.8-9.81 μH
r_i (i=1-12)	2.8-2.98 mΩ
L_{ij} (i,j=1-12)	9.78-9.8 μH
Volume	6420 mm^3

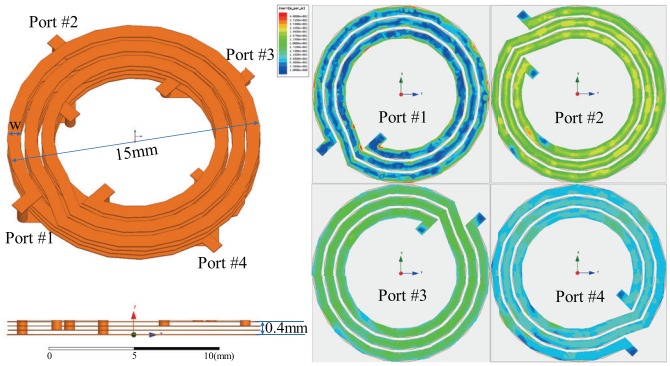

Fig. 12. FEM of the 13.56 MHz 4-winding transformer implemented on a four layer flexible PCB. The simulated current distribution on the four coils are also shown.

comprising four identical windings. Table I lists the parameters of the 200 kHz multiwinding transformer. L_i and r_i are the self-inductance and equivalent series resistance (ESR) at 200 kHz. L_{ij} is the inductance between port i and port j.

Switching at a few MHz enables air coupling with miniaturized size for the cell-level balancer. The air-coupled windings should be designed carefully to achieve the required mutual inductance with low ac winding resistance. Fig. 12 shows the ANSYS model of a 4-port 13.56-MHz multiwinding transformer which is built with four vertical-stacked coils. The transformer outer diameter is 15 mm and the overall thickness of the transformer is around 0.4 mm. The transformer can be implemented on flexible Kapton PCB.

The simulated current distribution on the four coils of the 13.56 MHz multiwinding transformer is also shown in Fig. 12. The current of each coil is evenly distributed on the surface of the coil trace, which helps reduce the ac winding resistance of the MHz transformer. Table II lists the key parameters of the MHz multiwinding transformer. Flexible magnetic sheets can be attached to the top and bottom layers of the transformer windings to shield the electromagnetic field and improve the mutual inductance if needed. It can be seen from Table II that the volume of the MHz multiwinding transformer is very small (71 mm^3) compared with that of the kHz transformer (6420 mm^3) due to its thin thickness (magnetic core free). The small volume of the MHz multiwinding transformer enables the compact integration between the MHz cell-level balancers and battery cells. The magnetic-free design improves robustness.

TABLE II
PARAMETERS OF THE MHz MULTIWINDING TRANSFORMER

Transformer Parameters (13.56 MHz)	Description
Number of turns (N)	3
Trace width (w)	0.75 mm
Trace gap (g)	0.25 mm
Trace thickness	35 μm
L_i (i=1-4)	144-147 nH
r_i (i=1-4)	0.3-0.34 Ω
L_{ij} (i,j=1-4)	107-128 nH
Volume	71 mm^3

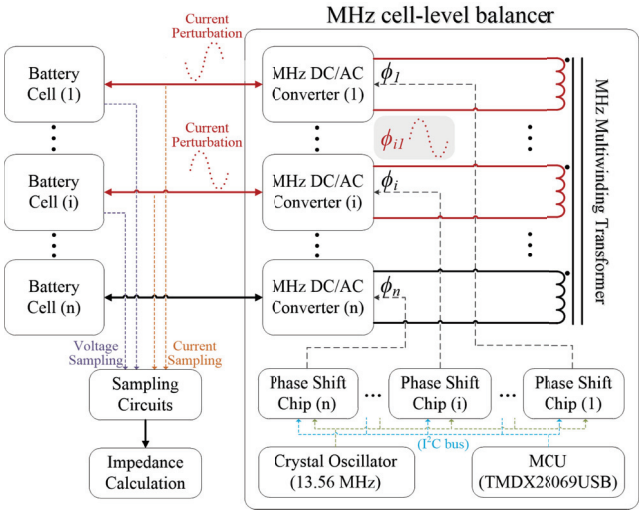

(a)

Fig. 13. Principles of the EIS function of the cell-level balancer.

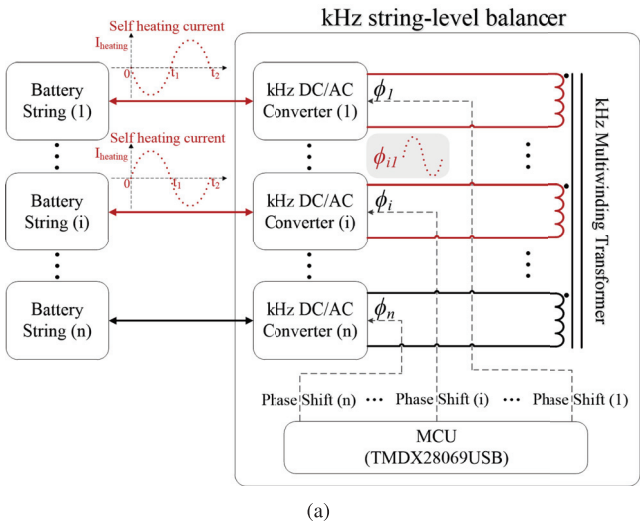

(a)

Fig. 14. Principles of the self-heating operation of the string-level balancer.

V. EIS AND SELF-HEATING MECHANISMS

A unique feature of the dual frequency MMB architecture is its capabilities of performing EIS at high frequencies on the cell-level and performing battery self-heating at low frequencies on the string-level. We explain the operation mechanisms of the EIS and self-heating functions in detail.

A. Cell-Level EIS Measurement

Fig. 13 illustrates the principles of the EIS function of the cell-level balancer. By changing the phase difference between two MHz inverters/rectifiers periodically, e.g., the phase difference between ϕ_1 and ϕ_i, a sinusoidal perturbation current is synthesized between two battery cell #1 and cell #i, as shown in Fig. 13. By changing the periods of the phase difference, the frequency and amplitude of the sinusoidal perturbation current can be modulated. We adopted a commercial phase delay IC DS1023-25 to implement the phase shift control in the MHz range. A crystal oscillator (SG-210STF 13.5600 M from Epson Timing) was used to provide the 13.56 MHz signal for the phase delay IC to drive the MHz inverters/rectifiers. A lookup table of the phase shift values was implemented in a microcontroller TMDX28069USB to generate the sinusoidal perturbation at different frequencies. The desired phase shift values are send to the multiple phase delay chips by the I^{2}C bus. In most of the existing work [14]–[17], an external power supply is required to generate the current perturbation with a limited bandwidth. The MHz cell-level balancer in the MMB architecture can generate the sinusoidal perturbation current with a wide range of frequencies, benefiting from the high switching frequency (i.e., 13.56 MHz).

As shown in Fig. 13, when the current perturbation is generated and applied on the cell #1 and cell #i, the voltage perturbations are excited correspondingly on the two battery cells, namely the battery ac voltages. Then, the waveforms of the current perturbations and the battery ac voltages of the two battery cells can be sampled by the voltage and current sampling circuits, and the sampling results are send to a processor or a microcontroller for the battery ac impedance calculation. To prove the concept, the waveforms of the sinusoidal current perturbation and battery ac voltage are captured by an oscilloscope. The battery ac impedances are calculated by applying fast Fourier transformation (FFT) to the measured voltage and current waveforms.

B. String-Level Self-Heating

Fig. 14 illustrates the principles using battery string #1 and battery string #i to perform the self-heating function. A microcontroller TMDX28069USB was used to create the PWM gate driving signals and modulate the phase shift of the driving singles for the kHz string-level balancer to perform the self-heating operation as well as balancing the battery strings. A sinusoidal current for the self-heating can be generated between string #1 and string #i by modulating the phase difference of the gate driving signals between two kHz inverters/rectifiers periodically, e.g., the phase difference between ϕ_1 and ϕ_i. A lookup table of the phase shift values was implemented in the microcontroller to generate the sinusoidal heating current across a frequency range.

From time 0 to time t_1, string #i discharges. Current flows through the kHz MAB converter to charge string #1. During time t_1 to time t_2, string #1 discharges. Current flows through the kHz MAB converter to charge String #i. The ac heating

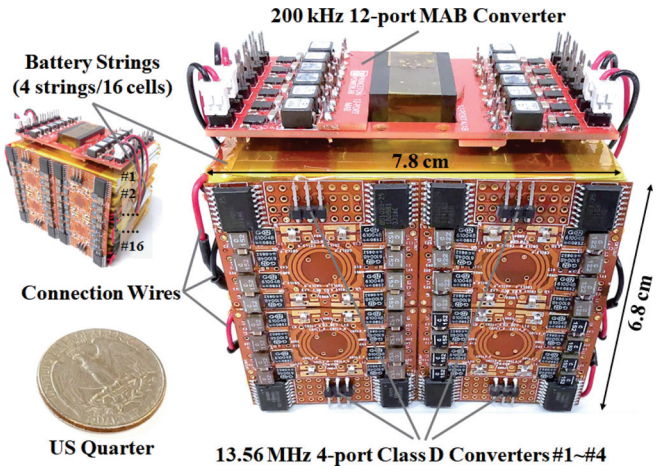

Fig. 15. Prototype dual frequency hierarchical MMB with EIS and self-heating.

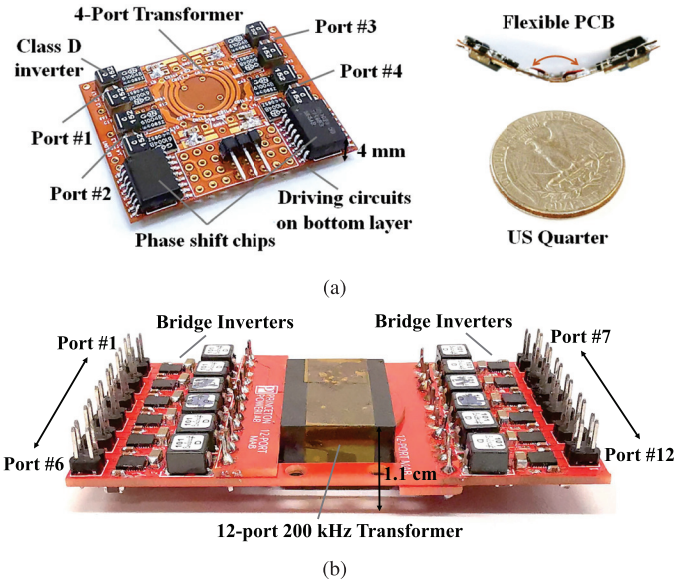

Fig. 16. Converters used in the MMB balancer. (a) 13.56-MHz 4-port CM Class-D converter. (b) 200-kHz 12-port MAB converter.

current is circulating between string #1 and string #i to heat up each other. During one switching cycle, each battery string discharges on one half-cycle and is charged on the other half-cycle. Due to the discharging and charging operation, the two battery strings equally share the energy consumption for heating and will maintain equal SOC. If the balancing current waveform is pure ac without dc bias, the self-heating process consumes balanced energy on both strings and leads to similar SOC change. If the current has dc bias or is asymmetry, the self-heating process leads to unbalanced SOC change. The battery balancing process can be integrated together with self-heating and EIS measurement functions.

VI. Experimental Results

Fig. 15 shows an MMB prototype with one 200-kHz 12-port MAB converter and four 13.56-MHz 4-port CM Class-D converters. The circuit topology is shown in Fig. 4. The balancer supports 16 battery cells which are grouped into four strings. The 200-kHz MAB converter balances the four battery strings. Four 13.56 MHz CM Class-D converters perform cell-to-cell balancing. The balancers are co-packaged together with the batteries.

Fig. 16(a) shows the 4-port 13.56-MHz CM Class-D converter. It consists of four active CM Class-D inverters, a 4-port air-core multiwinding transformer, the control and gate drive circuits. The power rating of the Class-D converter is 30 W. Eight GaN transistors, GS61004B, are used as the switches of the four Class-D inverters. The CM Class-D converter was built on a flexible PCB, as shown in Fig. 16(a), benefiting from the high switching frequency and air-coupled windings. A crystal oscillator (SG-210STF 13.5600 M from Epson Timing) was used to create the 13.56 MHz clock for the phase delay IC to drive the MHz inverters/rectifiers. The circuit performs cell-level balancing and high frequency current perturbation for EIS. The transformer parameters, e.g., number of turns N, trace width w, trace gap g, and trace thickness, are the same as listed in Table II. Fig. 16(b) shows a 200-kHz 12-port MAB converter. It consists of 12 half-bridge inverters and a 12-port multiwinding transformer with 3 vertical stacked PCBs. The MAB converter can balance up to 12 battery strings and the power rating of the converter is 300 W. Twelve 24-V DrMOSs, BQ500101, are used as the switches of the half-bridge inverters. Table I listed the key parameters of the 200-kHz transformer.

Fig. 17(a) shows the balancing process when the four 13.56-MHz CM Class-D inverters are balancing four battery cells. The initial voltages of the cells are different. The phase shift of the four active Class-D inverters is used to control the power flow among the battery cells. A CompactDAQ system controlled by Labview is used to capture the voltage data during the balancing process. All cell voltages converge after about 33 mins. Fig. 17(b) shows the balancing process when the 200 kHz MAB converter is balancing four battery strings. All cell voltages converge after about 65 mins by using the phase shift based power flow control. Fig. 18 shows the end to end efficiencies of the 13.56-MHz CM Class-D converter and the 200-kHz MAB converter. The peak cell-to-cell efficiency of the 13.56-MHz balancer is 74%. The peak string-to-string efficiency of the 200-kHz MAB balancer is 93%. In the balancing experiments, the battery cell and string voltages are used as the feedback for the balancing operation and the phase shifts of the cell-level and string-level balancers are modulated to control the multiway MIMO power flow for the cell-level and string-level balancing.

The 13.56-MHz cell-level balancer was used to perform EIS on a ICR18650 Li-ion battery cell. By sweeping the phase difference among the multiple inverters, the impedance of the battery cell is measured across a wide range of frequencies. Fig. 19(a) shows a 10 kHz sinusoidal current generated by the 13.56-MHz balancer. By applying FFT to the measured waveforms, the fundamental components of the battery ac voltage and current can be extracted to infer the battery impedance. Fig. 19(b)

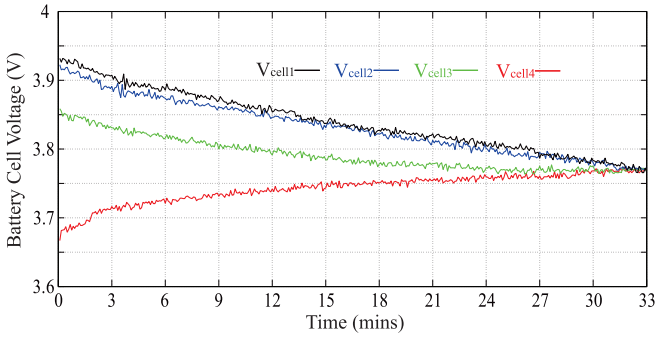

(a)

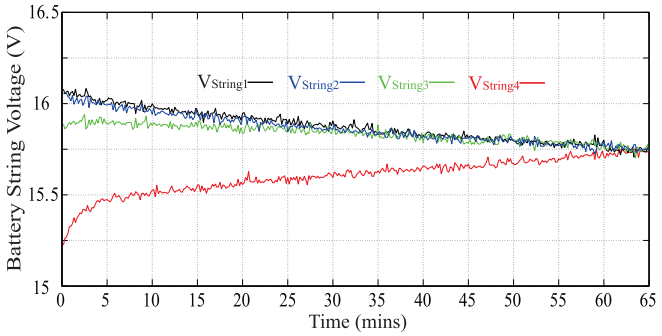

(b)

Fig. 17. Experimental results of the balancing operation. (a) Battery cells balancing operation using the 13.56-MHz CM Class-D converter. (b) Battery strings balancing operation using the 200-kHz MAB converter.

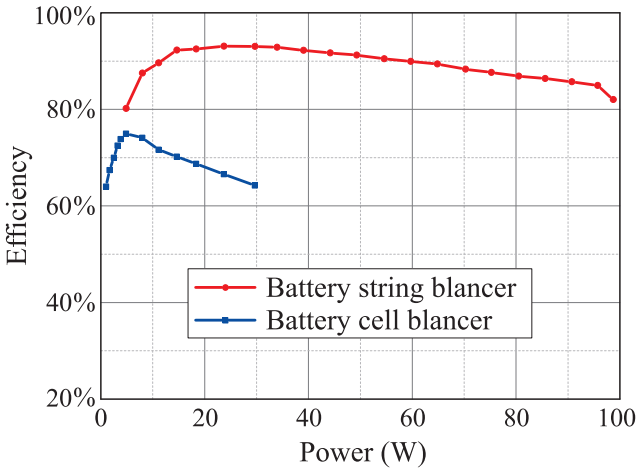

Fig. 18. End-to-end measured efficiency of the 13.56-MHz CM Class-D converter (cell balancer) and the 200-kHz MAB converter (string balancer).

compares the Nyquist plots illustrating the EIS measurement results from the prototype and a commercial instrument, where good match was found.

Similarly, the 200-kHz string-level balancer can perform self-heating across a wide range of frequencies. Two battery strings are used to heat each other. Each battery string comprises four series-connected Li-ion battery cells. Fig. 20 shows the current waveforms for self-heating at 100 Hz, 4.8 kHz, and 18 kHz, respectively. These waveforms are measured when the battery temperatures all start from 0°C. The battery string voltage and the cell voltage before heating are about 16 and 4 V, respectively.

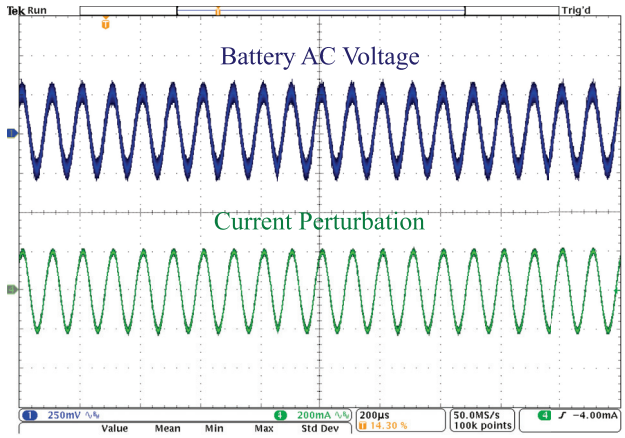

(a)

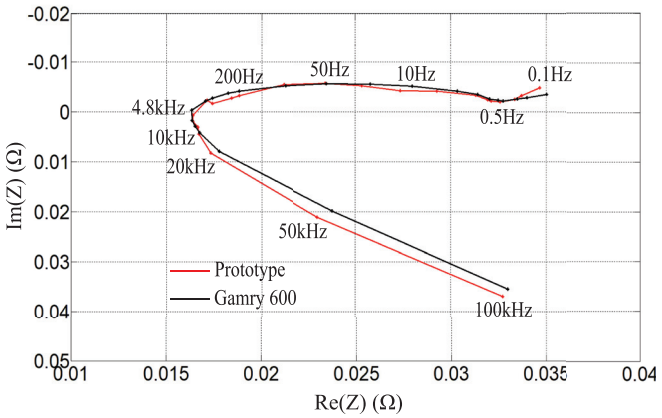

(b)

Fig. 19. (a) 10 kHz sinusoidal current generated by the 13.56-MHz CM Class-D converter for EIS measurement. (b) EIS measurement results of the prototype and a commercial instrument (Gamry Reference 600).

The amplitude of the sinusoidal voltage perturbation of the battery string, ΔV, is set at 0.8 V (peak to peak 1.6 V) to guarantee upper safe operation voltages (16.8 and 4.2 V) and lower safe operation voltages (12 and 3 V) for the battery strings and cells. Fig. 21 shows the measured battery temperature during a battery heating process with a room temperature of 15°C, which validates the self-heating capability of the MMB balancer. With the same ΔV, a smaller battery resistance (R) will lead to a high input heating power for the battery, which explains the fast heating speed at 4.8 kHz. Note the tested battery has a lower resistance at 4.8 kHz than those of 18 kHz and 100 Hz according to the EIS measurement results in Fig. 19. It is reported in [44]–[48] that heating the battery at high frequency (i.e., pure ohmic resistive frequency), such as 4.8 kHz, can reduce the battery degradation because of the reduced faradic current during the self-heating process. Note if a constant current is applied for the self-heating at the three frequencies, the low frequency, e.g., 100 Hz, will achieve a high heating speed due to the high heating power caused by the higher battery resistance.

Table III compares the proposed MMB architecture against a few existing hierarchical multilayer battery balancer techniques. To the best of our knowledge, this is the first work that explored

TABLE III
FEW EXISTING HIERARCHICAL MULTILAYER BATTERY BALANCER ARCHITECTURES

Publication	[35]	[36]	[37]	[38]	[39]	This work
Cell-level balancing	Yes	Yes	Yes	Yes	Yes	MIMO cells balancing
String-level balancing	Yes	Yes	Yes	Yes	Yes	MIMO strings balancing
Operating frequency	100 kHz to 120 kHz	N/A	10 kHz	250 kHz	100 kHz	200 kHz & 13.56 MHz
Peak efficiency	90.4%	N/A	N/A	93.5%	89.4%	93% (string-level balancing)
EIS measurement	No	No	No	No	No	Yes (Bandwidth: 0.1 Hz to 100 kHz)
Self-heating	No	No	No	No	No	Yes (Bandwidth: 100 Hz to 18 kHz)

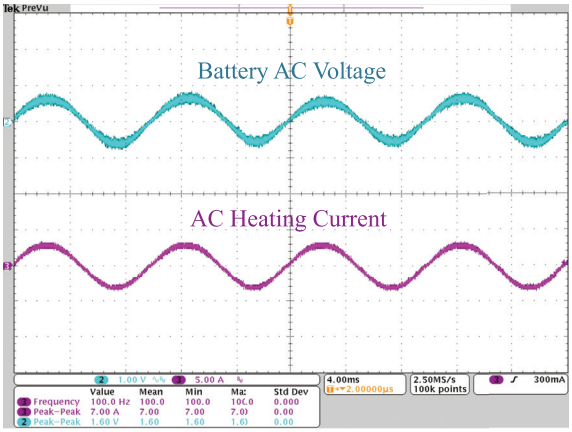

(a)

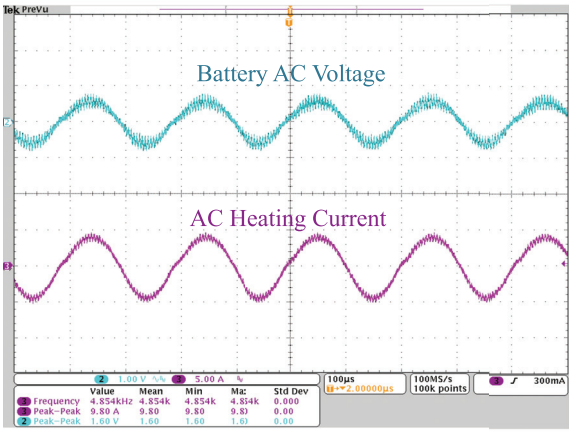

(b)

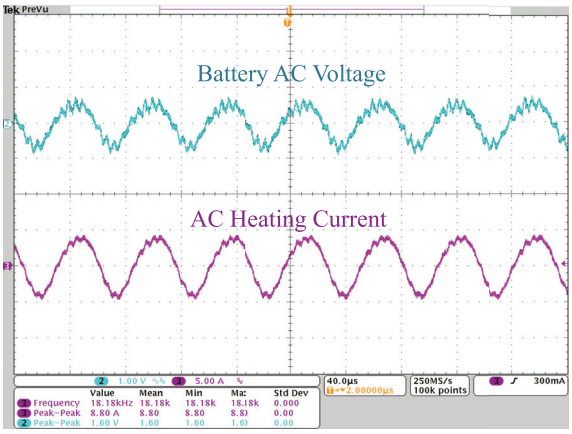

(c)

Fig. 20. Measured waveforms of the self-heating process. (a) Heating current at 100 Hz. (b) Heating current at 4.8 kHz. (c) Heating current at 18 kHz.

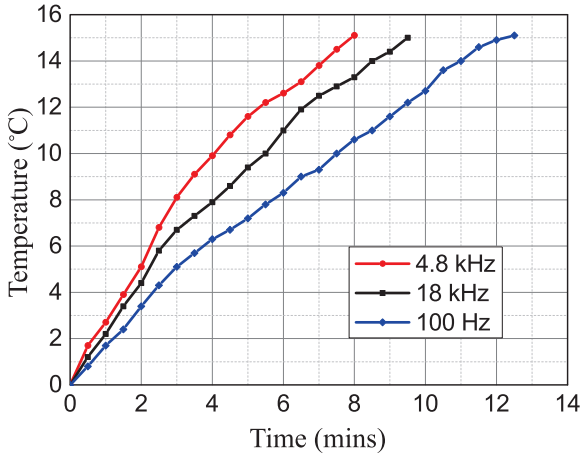

Fig. 21. Temperature rise of the battery strings in self-heating using current with different frequencies while maintaining the same voltage ripple ΔV.

the feasibility of implementing a multilayer battery balancing architecture with dual band operating frequencies, targeting both EIS measurement and battery self-heating functions. The 200-kHz 12-winding MAB design achieves among the highest string-to-string efficiency (93%), and the 13.56-MHz CM Class-D design is miniaturized and only requires air-coupled windings. The MIMO power flow control strategies of the voltage source driven MAB converter and the current source driven CM Class-D converter are applicable to a wide range of MIMO power converter architecture beyond battery balancing applications, such as multiport wireless power transfer.

VII. CONCLUSION

This article presents a dual frequency MMB architecture with integrated EIS and self-heating capabilities. The dual frequency MMB architecture enables MIMO balancing operation in the string-level and cell-level, and merges the advantages of kHz MAB converter and MHz CM Class-D converter. It also helps to eliminate the coupling influence among the cells in different strings and highly reduces the complexity of the balancer control. The MHz balancer enables cell-level EIS measurement with reduced size. The kHz balancer enables effective battery self-heating and string balancing. An MMB prototype with one 12-port 200-kHz string-to-string balancer and four 4-port 13.56-MHz cell-to-cell balancers is built and tested with a battery string comprising 16 battery cells, demonstrating the capabilities of integrated EIS, self-heating, and multilayer balancing.

ACKNOWLEDGMENT

This article was jointly supported by the Princeton E-ffiliates Partnership program, the DOE ARPA-E CIRCUITS program, and the National Science Foundation under Grant 1847365.

REFERENCES

[1] M. Liu, P. Wang, Y. Guan, and M. Chen, "A 13.56 MHz multiport-wireless-coupled (MWC) battery balancer with high frequency online electrochemical impedance spectroscopy," in *Proc. IEEE Energy Convers. Congr. Expo.*, 2019, pp. 537–544.

[2] Y. Elasser, Y. Chen, P. Wang, and M. Chen, "Sparse operation of multi-winding transformer in multiport-ac-coupled converters," in *Proc. 20th Workshop Control Model. Power Electron.*, 2019, pp. 1–8.

[3] J. Cao, N. Schofield, and A. Emadi, "Battery balancing methods: A comprehensive review," in *Proc. IEEE Vehicle Power Propulsion Conf.*, 2008, pp. 1–6.

[4] J. Rocabert, R. Capo-Misut, R. S. Munoz-Aguilar, J. I. Candela, and P. Rodriguez, "Control of energy storage system integrating electrochemical batteries and supercapacitors for grid-connected applications," *IEEE Trans. Industry Appl.*, vol. 55, no. 2, pp. 1853–1862, Mar./Apr. 2019.

[5] A. Khaligh and Z. Li, "Battery, ultracapacitor, fuel cell, and hybrid energy storage systems for electric, hybrid electric, fuel cell, and plug-in hybrid electric vehicles: State of the art," *IEEE Trans. Veh. Technol.*, vol. 59, no. 6, pp. 2806–2814, Jul. 2010.

[6] C. Kim, M. Kim, and G. Moon, "A modularized charge equalizer using a battery monitoring IC for series-connected li-ion battery strings in electric vehicles," *IEEE Trans. Power Electron.*, vol. 28, no. 8, pp. 3779–3787, Aug. 2013.

[7] L. Maharjan, T. Yamagishi, and H. Akagi, "Active-power control of individual converter cells for a battery energy storage system based on a multilevel cascade PWM converter," *IEEE Trans. Power Electron.*, vol. 27, no. 3, pp. 1099–1107, Mar. 2012.

[8] C. Lim, K. Lee, N. Ku, D. Hyun, and R. Kim, "A modularized equalization method based on magnetizing energy for a series-connected lithium-ion battery string," *IEEE Trans. Power Electron.*, vol. 29, no. 4, pp. 1791–1799, Apr. 2014.

[9] A. Jossen, "Fundamentals of battery dynamics," *J. Power Sources*, vol. 154, no. 2, pp. 530–538, 2006.

[10] G. L. Plett, "Sigma-point Kalman filtering for battery management systems of LIPB-based HEV battery packs: Part 1: Introduction and state estimation," *J. Power Sources*, vol. 161, no. 2 pp. 1356–1368, 2006.

[11] J. Remmlinger, M. Buchholz, M. Meiler, P. Bernreuter, and K. Dietmayer, "State-of-health monitoring of lithium-ion batteries in electric vehicles by on-board internal resistance estimation," *J. Power Sources*, vol. 196, no. 12, pp. 5357–5363, Jun. 2011.

[12] P. A. Cassani and S. S. Williamson, "Design, testing, and validation of a simplified control scheme for a novel plug-in hybrid electric vehicle battery cell equalizer," *IEEE Trans. Ind. Electron.*, vol. 57, no. 12, pp. 3956–3962, Dec. 2010.

[13] W. Waag, S. Kabitz, and D. U. Sauer, "Experimental investigation of the lithium-ion battery impedance characteristic at various conditions and aging states and its influence on the application," *Appl. Energy*, vol. 102, pp. 885–897, Feb. 2013.

[14] W. Huang and J. A. Abu Qahouq, "An online battery impedance measurement method using dc-dc power converter control," *IEEE Trans. Ind. Electron.*, vol. 61, no. 11, pp. 5987–5995, Nov. 2014.

[15] Y. Lee, S. Park, and S. Han, "Online embedded impedance measurement using high-power battery charger," *IEEE Trans. Ind. Appl.*, vol. 51, no. 1, pp. 498–508, Jan.–Feb. 2015.

[16] R. Koch, R. Kuhn, I. Zilberman, and A. Jossen, "Electrochemical impedance spectroscopy for online battery monitoring—Power electronics control," in *Proc. 16th Eur. Conf. Power Electron. Appl.*, 2014, pp. 1–10.

[17] D. A. Howey, P. D. Mitcheson, V. Yufit, G. J. Offer, and N. P. Brandon, "Online measurement of battery impedance using motor controller excitation," *IEEE Trans. Veh. Technol.*, vol. 63, no. 6, pp. 2557–2566, Jul. 2014.

[18] E. Din, C. Schaef, K. Moffat, and J. T. Stauth, "A scalable active battery management system with embedded real-time electrochemical impedance spectroscopy," *IEEE Trans. Power Electron.*, vol. 32, no. 7, pp. 5688–5698, Jul. 2017.

[19] M. C. Smart, B. V. Ratnakumar, and S. Surampudi, "Electrolytes for low-temperaturelithium batteries based on ternary mixtures of aliphatic carbonates," *J. Electrochem. Soc.*, vol. 146, pp. 486–492, 1999.

[20] S. S. Zhang, K. Xu, and T. R. Jow, "Low temperature performance of graphite electrode in Li-ion cells," *Electrochimica Acta*, vol. 48, 2002, pp. 241–246.

[21] S. S. Zhang, K. Xu, and T. R. Jow, "The low temperature performance of Li-ion batteries," *J. Power Sources*, vol. 115, 2003, pp. 137–140.

[22] J. Zhang, H. Ge, Z. Li, and Z. Ding, "Internal heating of lithium-ion batteries using alternating current based on the heat generation model in frequency domain," *J. Power Sources*, vol. 273, pp. 1030–1037, Jan. 2015.

[23] J. Jiang *et al.*, "A reduced low-temperature electro-thermal coupled model for lithium-ion batteries," *Appl. Energy*, vol. 177, pp. 804–816, Sep. 2016.

[24] S. Mohan, Y. Kim, and A. G. Stefanopoulou, "Energy-conscious warm-up of li-ion cells from subzero temperatures," *IEEE Trans. Ind. Electron.*, vol. 63, no. 5, pp. 2954–2964, May 2016.

[25] H. Ruan *et al.*, "A rapid low-temperature internal heating strategy with optimal frequency based on constant polarization voltage for lithium-ion batteries," *Appl. Energy*, vol. 177, pp. 771–782, Sep. 2016.

[26] T. A. Stuart and A. Hande, "HEV battery heating using ac currents," *J. Power Sources*, vol. 129, pp. 368–378, Apr. 2004.

[27] Y. Shang, B. Xia, N. Cui, C. Zhang, and C. C. Mi, "An automotive onboard ac heater without external power supplies for lithium-ion batteries at low temperatures," *IEEE Trans. Power Electron.*, vol. 33, no. 9, pp. 7759–7769, Sep. 2018.

[28] Y. Shang, C. Zhu, Y. Fu, and C. C. Mi, "An integrated heater equalizer for lithium-ion batteries of electric vehicles," *IEEE Trans. Ind. Electron.*, vol. 66, no. 6, pp. 4398–4405, Jun. 2019.

[29] Y. Shang, K. Liu, N. Cui, Q. Zhang, and C. Zhang, "A sine-wave heating circuit for automotive battery self-heating at subzero temperatures," *IEEE Trans. Ind. Informat.*, vol. 16, no. 5, pp. 3355–3365, May 2020.

[30] Y. Shang, K. Liu, N. Cui, N. Wang, K. Li, and C. Zhang, "A compact resonant switched-capacitor heater for lithium-ion battery self-heating at low temperatures," *IEEE Trans. Power Electron.*, vol. 35, no. 7, pp. 7134–7144, Jul. 2020.

[31] Y. Levron, D. R. Clement, B. Choi, C. Olalla, and D. Maksimovic, "Control of substring integrated converters in the isolated-port differential power-processing photovoltaic architecture," *IEEE J. Emerg. Sel. Topics Power Electron.*, vol. 2, no. 4, pp. 821–832, Dec. 2014.

[32] E. Candan, P. Shenoy, and R. Pilawa-Podgurski, "A series-stacked power delivery architecture with isolated differential power conversion for data centers," *IEEE Trans. Power Electron.*, vol. 31, no. 5, pp. 3690–3703, May 2016.

[33] M. Evzelman, M. M. Ur Rehman, K. Hathaway, R. Zane, D. Costinett, and D. Maksimovic, "Active balancing system for electric vehicles with incorporated low-voltage bus," *IEEE Trans. Power Electron.*, vol. 31, no. 11, pp. 7887–7895, Nov. 2016.

[34] P. Wang and M. Chen, "Towards power FPGA: Architecture, modeling and control of multiport power converters," in *Proc. IEEE Workshop Control Model. Power Electron.*, 2018, pp. 1–8.

[35] Z. Zhang, H. Gui, D. Gu, Y. Yang, and X. Ren, "Hierarchical active balancing architecture for lithium-ion batteries," *IEEE Trans. Power Electron.*, vol. 32, no. 4, pp. 2757–2768, Apr. 2017.

[36] B. Dong, Y. Li, and Y. Han, "Parallel architecture for battery charge equalization," *IEEE Trans. Power Electron.*, vol. 30, no. 9, pp. 4906–4913, Sep. 2015.

[37] S. Wang, L. Kang, X. Guo, Z. Wang, and M. Liu, "A novel layered bidirectional equalizer based on a buck-boost converter for series-connected battery strings," *Energies*, vol. 10, 2017, Art. no. 1011.

[38] F. Mestrallet, L. Kerachev, J. C. Crebier, and A. Collet, "Multiphase interleaved converter for lithium battery active balancing," *IEEE Trans. Power Electron.*, vol. 29, no. 6, pp. 2874–2881, Jun. 2014.

[39] F. Peng, H. Wang, and L. Yu, "Analysis and design considerations of efficiency enhanced hierarchical battery equalizer based on bipolar CCM buck-boost units," *IEEE Trans. Ind. Appl.*, vol. 55, no. 4, pp. 4053–4063, Jul./Aug. 2019.

[40] P. Wang, Y. Chen, P. Kushima, Y. Elasser, M. Liu, and M. Chen, "A 99.7% efficient 300 w hard disk drive storage server with multiport ac-coupled differential power processing (mac-DPP) architecture," in *Proc. IEEE Energy Convers. Congr. Expo.*, 2019, pp. 5124–5131.

[41] Y. Chen, P. Wang, H. Li, and M. Chen, "Power flow control in multi-active-bridge converters: Theories and applications," in *Proc. IEEE Appl. Power Electron. Conf. Expo.*, 2019, pp. 1500–1507.

[42] A. M. Imtiaz and F. H. Khan, "Time shared flyback converter based regenerative cell balancing technique for series connected li-ion battery strings," *IEEE Trans. Power Electron.*, vol. 28, no. 12, pp. 5960–5975, Dec. 2013.

[43] Y. Chen, P. Wang, Y. Elasser, and M. Chen, "LEGO-MIMO architecture: A universal multi-input multi-output (MIMO) power converter with linear extendable group operated (lego) power bricks," in *Proc. IEEE Energy Convers. Congr. Expo.*, 2019, pp. 5156–5163.
[44] Y. Ji and C. Wang, "Heating strategies for li-ion batteries operated from subzero temperatures," *Electrochim Acta*, vol. 107, pp. 664–74, 2013.
[45] S. Li, B. Wang, H. Peng, and X. Hua, "An electrochemistry-based impedance model for lithium-ion batteries," *J. Power Sources*, vol. 258, pp. 5357–5363, Jul. 2014.
[46] V. Agubra and J. Fergus, "Lithium ion battery anode aging mechanisms," *Materials* (Basel), vol. 6, no. 4, pp. 1310–1325, Mar. 2013.
[47] H. Ge, J. Huang, J. Zhang, and Z. Li, "Temperature-adaptive alternating current preheating of lithium-ion batteries with lithium deposition prevention," *J. Electrochem. Soc.*, vol. 163, no. 2, pp. 290–299, 2016.
[48] S. Boroujeni and K. Birke, "Study of a li-ion cell kinetics in five regions to predict li plating using a pseudo two-dimensional model," *Sustainability*, vol. 11, no. 22, pp. 1–14, Nov. 2019.

Ming Liu (Member, IEEE) received the B.S. degree from Sichuan University, Sichuan, China, in 2007, and the Ph.D. degree in electrical and computer engineering from the University of Michigan-Shanghai Jiao Tong University Joint Institute, Shanghai Jiao Tong University, Shanghai, China, in 2017.

He is currently a Postdoctoral Research Fellow with the Department of Electrical Engineering, Princeton University, Princeton, NJ, USA. His research interests include circuit topology and architecture, control strategy, optimization-based design methods for MHz wireless power transfer, and high frequency power electronics.

Dr. Liu was the recipient of the Top-10 Academic Star Award and Excellent PhD Thesis Award Nomination at Shanghai Jiao Tong University, and the Research Excellence Award from AirFuel Alliance.

Yenan Chen (Member, IEEE) received the bachelor's and Ph.D. degrees in electrical engineering from Zhejiang University, Hangzhou, China, in 2010 and 2018, respectively.

Since 2018, he has been a Postdoctoral Research Associate with the Department of Electrical Engineering, Princeton University, NJ, USA. His research interests include high frequency power converters, advanced power electronics architecture, grid-interface power electronics, point-of-load power converters, and renewable energy system. He holds three issued Chinese patents.

Dr. Chen was the recipient of the APEC Outstanding Presentation Award in 2019, and the First Place Award from the Innovation Forum of Princeton University in 2019.

Youssef Elasser (Student Member, IEEE) received the B.Sc. degree in electrical engineering and computer science with a concentration in electric power from Rensselaer Polytechnic Institute, Troy, NY, USA, in 2018. He is currently working toward the Ph.D. degree with Princeton University, Princeton, NJ, USA.

His research interests include renewable energy storage systems, grid-interface power electronics, and point of load power converters.

Mr. Elasser was the recipient of the Grainger Schoalrs Award for distinguished undergraduates studying electric power from the Rensselaer Polytechnic Institute, and the First Place Award from the 2019 Princeton Innovation Forum and the prestigious NSF Graduate Research Fellowship in 2020 from Princeton University.

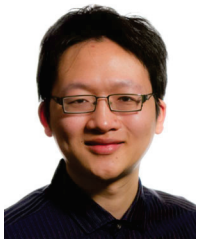

Minjie Chen (Senior Member, IEEE) received the B.S. degree from Tsinghua University, Beijing, China, in 2009, and the S.M., E.E., and Ph.D. degrees from Massachusetts Institute of Technology (MIT), Cambridge, MA, USA, in 2012, 2014, and 2015.

He was a Postdoctoral Research Associate with MIT in 2016. He joined the Department of Electrical Engineering and Andlinger Center for Energy and the Environment at Princeton University as an Assistant Professor in 2017, where he leads the Princeton Power Electronics Research Lab (PowerLab). His research interests include high frequency power electronics, advanced power electronics architectures, power magnetics, and the design of high performance power electronics for emerging and important applications.

Prof. Chen was the recipient of the NSF CAREER Award, the Dimitris N. Chorafas outstanding Ph.D. Thesis Award from MIT, two Transactions Prize Paper Awards and an Outstanding Reviewer Award from IEEE Transactions on Power Electronics, two IEEE ECCE Best Demonstration Awards, a Siebel Energy Institute Research Award, and the First Place Award from the Innovation Forum of Princeton University. He was honored by the *Princeton Engineering Commendation List for Outstanding Teaching*. He is an Associate Editor of IEEE TRANSACTIONS ON POWER ELECTRONICS, a Guest Associate Editor of IEEE JOURNAL OF EMERGING AND SELECTED TOPICS IN POWER ELECTRONICS, and an Associate Technical Program Committee Chair of IEEE Energy Conversion Congress and Exposition in 2019.